Jize Dai
Department of Mechanical Engineering,
Stanford University,
Stanford, CA 94305
e-mail: jizedai@stanford.edu

Lu Lu
Department of Mechanical Engineering,
Stanford University,
Stanford, CA 94305
e-mail: lulu2@stanford.edu

Sophie Leanza
Department of Mechanical Engineering,
Stanford University,
Stanford, CA 94305
e-mail: leanza@stanford.edu

John W. Hutchinson
School of Engineering and Applied Sciences,
Harvard University,
Cambridge, MA 02138
e-mail: hutchinson@husm.harvard.edu

Ruike Renee Zhao[1]
Department of Mechanical Engineering,
Stanford University,
Stanford, CA 94305
e-mail: rrzhao@stanford.edu

Curved Ring Origami: Bistable Elastic Folding for Magic Pattern Reconfigurations

Ring origami has emerged as a robust strategy for designing foldable and deployable structures due to its impressive packing abilities achieved from snap-folding. In general, polygonal rings with rationally designed geometric parameters can fold into compact three-loop configurations with curved segments which result from the internal bending moment in the folded state. Inspired by the internal bending moment-induced curvature in the folded state, we explore how this curvature can be tuned by introducing initial natural curvature to the segments of the polygonal rings in their deployed stress-free state, and study how this initial curvature affects the folded configurations of the rings. Taking a clue from straight-segmented polygonal rings that fold into overlapping curved loops, we find that this behavior can be reversed by introducing curvature into the ring segments in the stress-free initial state such that the rings fold into a looped straight-line configuration with "zero" area. This strategy realizes extreme packing of the rings. In this work, by a combination of experimental observation, finite element analysis, and theoretical modeling, we systematically study the effect of segment curvature on folding behaviors, folded configurations, and packing abilities of curved ring origami with different geometries. It is anticipated that curved ring origami can open a new avenue for the design of foldable and deployable structures with simple folded configurations and high packing efficiency.
[DOI: 10.1115/1.4062221]

Keywords: ring origami, curvature, snap-folding, packing ability, foldable structures, deployable structures

1 Introduction

Foldable and deployable structures have attracted great attention in recent decades due to their capabilities of shape reconfiguration and significant size change, which have found widespread engineering applications such as deployable aerospace structures [1,2], shape-morphing soft robots [3–5], and foldable medical devices [6]. Among the different folding strategies, mechanical instability has been intensively explored by utilizing the buckling and snap-through behaviors of structures for self-guided shape reconfiguration and size change [7–9]. Ring origami, a folding approach based on snap-through instability, has been demonstrated as a robust method for folding closed-loop rods of different geometries (such as polygons) under bending or twisting loads [10–12]. The snap-folding of well-designed ring origami can achieve high packing efficiency. For example, a hexagonal ring can snap-fold into a three-loop overlapping peach core-shaped configuration with only 10.6% of its initial area [13]. Additionally, it was recently found that introducing geometric modifications and residual strains to the ring can facilitate the folding of ring origami by only a point load or a localized twist with much reduced required energy input [14]. The packing efficiency of ring origami can be further enhanced by assembling multiple rings into two-dimensional (2D) tessellations or three-dimensional (3D) structures [15]. Due to these merits, ring origami is an ideal candidate to serve as the basis for foldable and deployable functional structures such as foldable solar panel devices [15], deployable space structures [16], flexible electronics [17], and foldable tents [18].

In general, polygonal rings with straight segments and rationally designed geometric parameters (cross-section shape, aspect ratio, span of the ring, etc.) can fold into three-loop configurations with curved segments (see Fig. 11 in Appendix A) which result from the internal bending moment in the folded state. The curvature of the folded ring can be fully predicted by the Kirchhoff rod model and finite element analysis (FEA) [10,19]. Inspired by the internal bending moment-induced curvature at the folded state, we have recently explored how this curvature can be tuned by introducing segments with initial natural curvature into the polygonal rings in their deployed stress-free state, and how this initial curvature affects the folded configurations of the rings. Although polygonal segments with both initial natural curvature and initial bending stress could be considered, only the role of initial natural curvature is studied here. Thus, in this paper, all the deployed rings are stress-free. An exciting discovery, which will be illustrated for several ring geometries, is that it is possible to choose an initial natural segment curvature such that the folded state is a pattern of straight loops with an idealized area of zero. In the remainder of this Introduction, several illustrations of the experimental observations explored later in the paper will be previewed to indicate the nature of the study and to whet the appetite of the reader for what follows.

In Fig. 1(*a*), a depiction of a straight-segmented hexagonal ring that can fold into a three-loop fully overlapping peach core configuration is given. Then, in Fig. 1(*b*), we show how a hexagon with segments having a particular natural curvature (defined later in the paper) folds into a nearly straight-sided three-loop ring. The photographs in Fig. 1 are of experimental realizations of the rings (see Movie 1 available in the Supplemental Materials on the ASME Digital Collection for the bistable elastic folding process and see Appendix B for details on the ring fabrication). In principle, the packing ratio (area of the folded state to area of the deployed state) of the curved ring can decrease to zero if the corner radius

[1]Corresponding author.

This paper is dedicated to Professor Kyung-Suk Kim, for his contributions to experimental and theoretical micro and nano-mechanics, and in celebration of his 70th birthday.

Contributed by the Applied Mechanics Division of ASME for publication in the Journal of Applied Mechanics. Manuscript received March 20, 2023; final manuscript received March 23, 2023; published online September 8, 2023. Assoc. Editor: Pradeep Sharma.

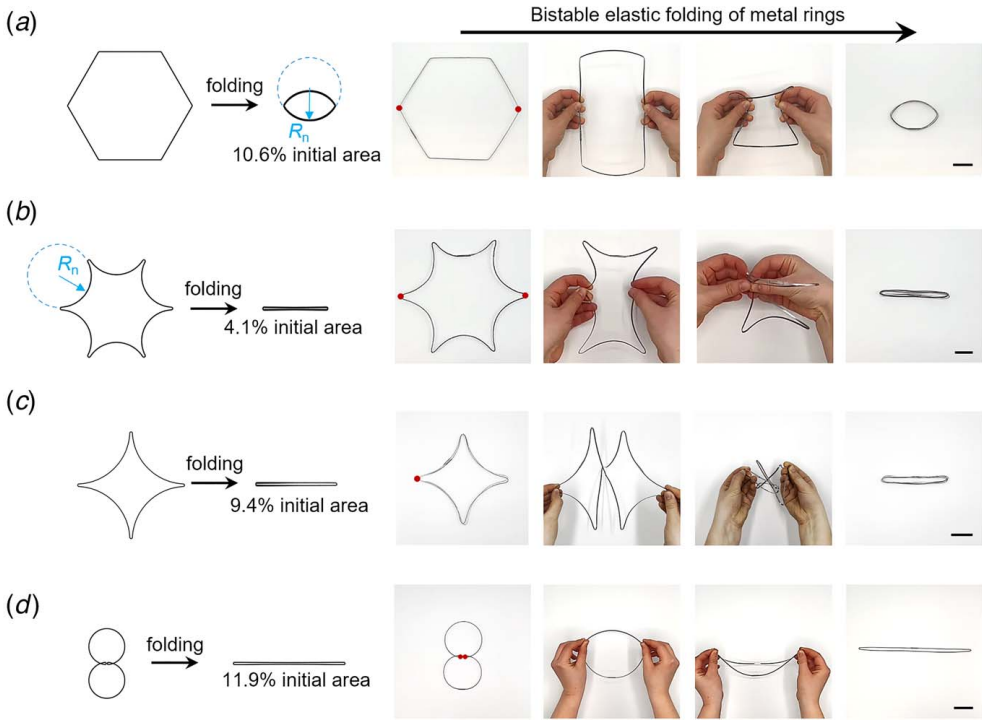

Fig. 1 Folding of ring origami with straight segments and curved segments that enables a high packing efficiency. (*a*) Single-layer hexagonal ring folds into a three-loop fully overlapping peach core shape with a segment radius of R_n. (*b*) Single-layer curved hexagonal ring folds into a three-loop straight-line geometry. Note that the curved hexagonal ring has the same segment length and the same segment curvature, $1/R_n$, as the folded configuration of a straight-segmented hexagonal ring. (*c*) Double-layer curved square ring folds into a four-loop straight-line geometry. (*d*) Single-layer "8"-shaped ring folds into a single-loop straight-line geometry. The initial and folded configurations on the left are obtained from FEA simulations, while the bistable elastic folding processes on the right are from experiments. The red dots denote the locations on the ring where bending moments are applied. Scale bars: 5 cm.

is negligible and the segment thickness is ignored. In our specimens, the corner radius, normalized by the segment radius (R_n), is 0.045 and the folded configuration of the curved hexagonal ring is 4.1% of its initial area, which is about 2.5 times smaller than the packing ratio of a hexagonal ring with straight segments (10.6%) [13]. A folded configuration with straight segments can also be obtained from a double-layer square ring (see Fig. 12 in Appendix B for fabrication details). As shown in Fig. 1(*c*), the double-layer square ring folds into a four-loop straight-line geometry, with a packing ratio of 9.4% with respect to the initial double-layer ring. Additionally, a single-loop straight-line configuration can be achieved by folding a single-layer "8"-shaped ring [20], which has a packing ratio of 11.9% (Fig. 1(*d*)). Motivated by such examples, the current work aims to study curved ring origami by investigating the effect of segment curvature on their folded configurations, snap-folding behaviors, and corresponding packing abilities.

Broadly speaking, curved ring origami encompasses slender structures with curved geometries that are widely seen in nature and engineering applications such as biological filaments [21], overhand knots [22], circular rings [11], and curved crease origami [23]. In these structures, curvature plays a significant role in their mechanical instabilities. It is worth noting that recent papers have studied the effect of curvature on the instabilities of rings or ring-like structures and found that curvature can induce residual stress and thus tune the stability and the folded configurations of circular rings [18,24,25], buckling and post-buckling patterns of creased annular elastic strips [26], and bistability and looping behaviors of creased annuli with discontinuities [27]. However, the focus of these previous studies is quite different from those in this paper, where the emphasis is on the role of the initial stress-free natural curvature of the polygonal ring segments. To our knowledge, there is no existing work that examines how the natural curvature of the polygonal ring segments affects the instability and folding behavior of 2D curved ring origami. As demonstrated in this paper, ring segments with stress-free natural curvature can generate a rich set of folding configurations worthy of further study.

This work combines experiments, FEA simulations, and theoretical modeling to systematically study the effect of natural segment curvature on the snap-folding of curved ring origami of different geometries. In addition to the single-layer curved hexagonal ring and double-layer curved square ring shown in Figs. 1(*b*) and 1(*c*), which can fold into straight-line loop configurations, we also study the variety of folded configurations achieved from single-layer curved octagonal rings and double-layer curved hexagonal rings with initial segment curvature. For each case, we present the initial and folded configurations, moment-bending angle curves, energy landscapes, packing ratios, and folding paths of the ring origami. It is anticipated that the current work will provide guidance for the design of foldable and deployable functional structures with simple folded configurations and high packing efficiency, for potential application in deployable aerospace structures, foldable electronics, and reconfigurable architecture.

The remainder of this paper is organized as follows. In Sec. 2, we describe the FEA and theoretical model used to study the snap-folding of curved ring origami. In Sec. 3, we study the effect of natural segment curvature on the folding behaviors and packing abilities of single-layer curved hexagonal rings and single-layer curved octagonal rings. In Sec. 4, we investigate the influence of segment curvature on the folding behaviors and packing abilities of double-layer curved square rings and double-layer curved hexagonal rings. Finally, in Sec. 5, we summarize the main findings of this work.

2 Method and Model

2.1 Finite Element Analysis. FEA simulations for the snap-folding of both single-layer and double-layer rings are conducted in the commercial software ABAQUS 2021 (Dassault Systèmes, France). All the simulated rings have a circumcircle radius of 200 mm, a cross-sectional thickness and height of 0.5 mm and 2 mm, respectively, and a corner radius of 5 mm. For all simulations, the C3D8R element is used with a mesh size of 0.1 mm. Young's Modulus and Poisson's ratio used are $E = 200$ GPa and $\nu = 0.3$, respectively. The boundary conditions at the loading points for single-layer and double-layer rings are not the same. For single-layer rings, a pair of bending angles are applied to both the left and right corners. For double-layer rings, the bending angles are applied on the left corners of both layers. In addition, a small damping is used to stabilize all simulations, which produces negligible energy dissipation (see Appendix C for details).

2.2 Theoretical Model. The Kirchhoff rod model has been widely used in modeling the mechanical behaviors of slender structures [28–31] and is adopted to study the snap-folding behaviors of ring origami with curved segments. A schematic of a naturally curved rod of length L, thickness t, and height h is shown in Fig. 2(*a*). The rod is assumed to be unshearable and inextensible, which means that the centerline of the rod is always perpendicular to the cross-section and the length of the rod remains unchanged during deformation. The deformation of the centerline can be described by a position vector $\mathbf{p}(s) = p_1\mathbf{E}_1 + p_2\mathbf{E}_2 + p_3\mathbf{E}_3$ in the global basis ($\mathbf{E}_1$, $\mathbf{E}_2$, $\mathbf{E}_3$), where $s \in [0, L]$ is the arc length coordinate. Moreover, a local basis [$\mathbf{e}_1(s)$, $\mathbf{e}_2(s)$, $\mathbf{e}_3(s)$] is attached to the centerline of the rod with $\mathbf{e}_1$ and $\mathbf{e}_2$ being unit vectors along the height direction and thickness direction, respectively, and $\mathbf{e}_3$ being the unit tangent vector of the centerline, which indicates $\mathbf{p}' = \mathbf{e}_3$. Throughout the paper, a prime denotes differentiation with respect to the arc length coordinate s, i.e., $(\cdot)' = d(\cdot)/ds$. The kinematics of the local basis is determined by $\mathbf{e}_i' = \boldsymbol{\omega} \times \mathbf{e}_i$ ($i = 1$, 2, 3), where $\boldsymbol{\omega} = \kappa_1\mathbf{e}_1 + \kappa_2\mathbf{e}_2 + \kappa_3\mathbf{e}_3$ is the Darboux vector, κ_1 and κ_2 are the bending curvatures, and κ_3 is the twisting curvature. Based on the Kirchhoff rod theory, in the absence of body forces and couples, the internal force $\mathbf{N}$ and moment $\mathbf{M}$ on the centerline of the rod satisfy

$$\begin{aligned} &\mathbf{N}' = \mathbf{0}, \\ &\mathbf{M}' + \mathbf{p}' \times \mathbf{N} = \mathbf{0} \end{aligned} \tag{1}$$

where $\mathbf{N} = N_1\mathbf{e}_1 + N_2\mathbf{e}_2 + N_3\mathbf{e}_3$ and $\mathbf{M} = M_1\mathbf{e}_1 + M_2\mathbf{e}_2 + M_3\mathbf{e}_3$. Projecting Eq. (1) along the local basis ($\mathbf{e}_1$, $\mathbf{e}_2$, $\mathbf{e}_3$) provides six equilibrium equations

$$\begin{aligned} &N_1' - N_2\kappa_3 + N_3\kappa_2 = 0 \\ &N_2' - N_3\kappa_1 + N_1\kappa_3 = 0 \\ &N_3' - N_1\kappa_2 + N_2\kappa_1 = 0 \\ &M_1' - M_2\kappa_3 + M_3\kappa_2 - N_2 = 0 \\ &M_2' + M_1\kappa_3 - M_3\kappa_1 + N_1 = 0 \\ &M_3' - M_1\kappa_2 + M_2\kappa_1 = 0 \end{aligned} \tag{2}$$

Considering linear constitutive relations, the internal moment can be written as

$$\mathbf{M} = EI_1(\kappa_1 - \kappa_1^{(0)})\mathbf{e}_1 + EI_2(\kappa_2 - \kappa_2^{(0)})\mathbf{e}_2 + GJ(\kappa_3 - \kappa_3^{(0)})\mathbf{e}_3 \tag{3}$$

where E and G are the Young's modulus and the shear modulus of the rod, respectively. $G = E/[2(1+\nu)]$, where ν is the Poisson's ratio. $I_1 = ht^3/12$ and $I_2 = h^3t/12$ are the moments of inertia, and J is the rotational constant. For a rod with a rectangular cross section, $J = \lambda ht^3/3$ with [32]

$$\lambda = 1 - \frac{192}{\pi^5}\frac{t}{h}\sum_{k=1}^{\infty}\frac{1}{(2k-1)^5}\tanh\left(\frac{(2k-1)\pi h}{2t}\right) \tag{4}$$

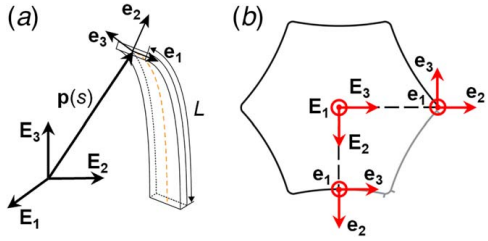

Fig. 2 Schematics of (*a*) the rod model and (*b*) a curved hexagonal ring. The local basis ($\mathbf{e}_1$, $\mathbf{e}_2$, $\mathbf{e}_3$) is attached to the centerlines of the rod and the ring, and the global basis ($\mathbf{E}_1$, $\mathbf{E}_2$, $\mathbf{E}_3$) is located at the center of the ring.

In Eq. (3), $\kappa_1^{(0)}$, $\kappa_2^{(0)}$, and $\kappa_3^{(0)}$ represent the initial bending curvatures and twisting curvature of the rod. In the present work, all rings stay in a plane without pre-twist in the initial state, and therefore $\kappa_2^{(0)} = \kappa_3^{(0)} = 0$.

Further, a unit quaternion $\mathbf{q}(s) = [q_0, q_1, q_2, q_3]$ is introduced to relate the local basis and the global basis [33,34], as

$$[\mathbf{e}_1, \mathbf{e}_2, \mathbf{e}_3]^T = [\mathbf{Q}][\mathbf{E}_1, \mathbf{E}_2, \mathbf{E}_3]^T \tag{5}$$

with

$$[\mathbf{Q}] = 2\begin{bmatrix} q_0^2 + q_1^2 - \frac{1}{2} & q_1q_2 + q_0q_3 & q_1q_3 - q_0q_2 \\ q_1q_2 - q_0q_3 & q_0^2 + q_2^2 - \frac{1}{2} & q_2q_3 + q_0q_1 \\ q_1q_3 + q_0q_2 & q_2q_3 - q_0q_1 & q_0^2 + q_3^2 - \frac{1}{2} \end{bmatrix} \tag{6}$$

Based on Eq. (5) and $\mathbf{p}' = \mathbf{e}_3$, one can obtain that

$$\begin{aligned} p_1' &= 2(q_1q_3 + q_0q_2) \\ p_2' &= 2(q_2q_3 - q_0q_1) \\ q_3' &= 2(q_0^2 + q_3^2) - 1 \end{aligned} \tag{7}$$

Taking the derivative of Eq. (5) and using $\mathbf{e}_i' = \boldsymbol{\omega} \times \mathbf{e}_i$, we have

$$\begin{aligned} q_0' &= (-q_1\kappa_1 - q_2\kappa_2 - q_3\kappa_3)/2 \\ q_1' &= (q_0\kappa_1 - q_3\kappa_2 + q_2\kappa_3)/2 \\ q_2' &= (q_3\kappa_1 + q_0\kappa_2 - q_1\kappa_3)/2 \\ q_3' &= (-q_2\kappa_1 + q_1\kappa_2 + q_0\kappa_3)/2 \end{aligned} \tag{8}$$

Equations (2), (7), and (8) provide thirteen governing equations for the rod, which include thirteen unknowns, i.e., the internal forces (N_1, N_2, N_3), the curvatures (κ_1, κ_2, κ_3), the position vector components (p_1, p_2, p_3), and the quaternion components (q_0, q_1, q_2, q_3). When supplemented with appropriate boundary conditions, the differential equation system forms a well-posed boundary value problem (BVP).

For ring origami consisting of polygons with curved segments and rounded corners, the natural curvatures at the joints of the segments and the corners are discontinuous, and therefore, the rings have to be divided into multiple segments such that each segment can be modeled as a Kirchhoff rod. The details of the curvature in the corner joints are not modeled, but, instead, conditions of continuity across the joints are imposed. Such a multi-segment rod model has recently been used to study the multi-stability of bigons and bigon rings (two-sided curved segment polygons) [35], snap-folding of ring origami with different geometries [19], and snap-folding of hexagonal ring origami with residual strain

and pre-twisted segments [14]. For a ring divided into m segments, there are $13m$ governing equations containing $13m$ unknown variables, which require $13m$ boundary conditions to produce a well-posed BVP. The variables for the jth segment of the rod are denoted by $[N_{ij}, \kappa_{ij}, p_{ij}, q_{0j}, q_{ij}]$ ($i = 1, 2, 3$, and $j = 1, 2, \cdots, m$), in which N_{ij} and κ_{ij} are defined in the local basis ($\mathbf{e}_1$, $\mathbf{e}_2$, $\mathbf{e}_3$) and p_{ij} is defined in the global basis ($\mathbf{E}_1$, $\mathbf{E}_2$, $\mathbf{E}_3$). For simplicity, we introduce the following quantities to normalize the relevant variables

$$\bar{N}_{ij} = \frac{N_{ij}R_0^2}{GJ},\ (\bar{\kappa}_{ij}, \bar{\kappa}_{ij}^{(0)}) = (\kappa_{ij}, \kappa_{ij}^{(0)})R_0,\ \bar{p}_{ij} = \frac{p_{ij}}{R_0}$$
$$\bar{s}_j = \frac{s_j}{R_0 l_j},\ \frac{d(\cdot)}{d\bar{s}_j} = R_0 l_j \frac{d(\cdot)}{ds_j} \tag{9}$$

where R_0 is the circumcircle radius of the curved segment ring, L_j is the length of the jth segment, and $l_j = L_j/R_0$ is a scaling factor that unifies the normalized arc length of different segments into the same range [0, 1]. By using these normalized quantities, the $13m$ governing equations for the multi-segment rod system can be written as

$$\begin{aligned}
&\bar{N}'_{1j} = (\bar{N}_{2j}\bar{\kappa}_{3j} - \bar{N}_{3j}\bar{\kappa}_{2j})l_j,\ \ \bar{N}'_{2j} = (\bar{N}_{3j}\bar{\kappa}_{1j} - \bar{N}_{1j}\bar{\kappa}_{3j})l_j\\
&\bar{N}'_{3j} = (\bar{N}_{1j}\bar{\kappa}_{2j} - \bar{N}_{2j}\bar{\kappa}_{1j})l_j\\
&\bar{\kappa}'_{1j} = (\bar{\kappa}_{1j}^{(0)})' + [(\beta-1)\bar{\kappa}_{2j}\bar{\kappa}_{3j} + \bar{N}_{2j}]l_j/\alpha\\
&\bar{\kappa}'_{2j} = -[\alpha(\bar{\kappa}_{1j} - \bar{\kappa}_{1j}^{(0)})\bar{\kappa}_{3j} - \bar{\kappa}_{3j}\bar{\kappa}_{1j} + \bar{N}_{1j}]l_j/\beta\\
&\bar{\kappa}'_{3j} = [\alpha(\bar{\kappa}_{1j} - \bar{\kappa}_{1j}^{(0)})\bar{\kappa}_{2j} - \beta\bar{\kappa}_{2j}\bar{\kappa}_{1j}]l_j\\
&\bar{p}'_{1j} = 2(q_{1j}q_{3j} + q_{0j}q_{2j})l_j,\ \ \bar{p}'_{2j} = 2(q_{2j}q_{3j} - q_{0j}q_{1j})l_j\\
&\bar{p}'_{3j} = (2q_{0j}^2 + 2q_{3j}^2 - 1)l_j\\
&q'_{0j} = (-q_{1j}\bar{\kappa}_{1j} - q_{2j}\bar{\kappa}_{2j} - q_{3j}\bar{\kappa}_{3j})l_j/2,\\
&q'_{1j} = (q_{0j}\bar{\kappa}_{1j} - q_{3j}\bar{\kappa}_{2j} + q_{2j}\bar{\kappa}_{3j})l_j/2\\
&q'_{2j} = (q_{3j}\bar{\kappa}_{1j} + q_{0j}\bar{\kappa}_{2j} - q_{1j}\bar{\kappa}_{3j})l_j/2,\\
&q'_{3j} = (-q_{2j}\bar{\kappa}_{1j} + q_{1j}\bar{\kappa}_{2j} + q_{0j}\bar{\kappa}_{3j})l_j/2
\end{aligned} \tag{10}$$

where α and β represent the bending-to-torsional rigidity ratios and are given by

$$\alpha = \frac{EI_1}{GJ} = \frac{1+\nu}{2\lambda},\quad \beta = \frac{EI_2}{GJ} = \frac{1+\nu}{2\lambda}\left(\frac{h}{t}\right)^2 \tag{11}$$

For single-layer hexagonal and octagonal rings studied here, we only need to take one-quarter of them for the analysis due to the symmetry, and then, the quarter rings are sub-divided into their curved segments ($m = 4$ for the hexagonal ring, as shown in Fig. 2(*b*), and $m = 5$ for the octagonal ring). In the present work, we apply bending loads to fold the ring, and thus, the corresponding boundary conditions at the left boundary of the first segment $\bar{s}_1 = 0$ should satisfy [14]

$$\bar{N}_{21} = 0,\quad \bar{p}_{11} = 0,\quad \bar{p}_{31} = 0,\quad \bar{\kappa}_{31} = 0,\quad q_{11} = 0,\quad q_{21} = 0 \tag{12}$$

and at the right boundary of the mth segment $\bar{s}_m = 1$, boundary conditions are

$$\begin{aligned}
&\bar{N}_{1m} = 0,\quad \bar{N}_{2m} = 0,\quad \bar{p}_{2m} = 0,\quad q_{0m} = \frac{\sqrt{2}}{2}\cos\left(\frac{\theta}{2}\right)\\
&q_{1m} = \frac{\sqrt{2}}{2}\cos\left(\frac{\theta}{2}\right),\quad q_{2m} = \frac{\sqrt{2}}{2}\sin\left(\frac{\theta}{2}\right),\quad q_{3m} = -\frac{\sqrt{2}}{2}\sin\left(\frac{\theta}{2}\right)
\end{aligned} \tag{13}$$

Here, θ is the bending angle at the loading positions. Additionally, by considering the force equilibrium and geometric compatibility at the joints of adjacent segments, we can obtain $12(n-1)$ continuous boundary conditions for $\bar{N}_{1j}$, $\bar{N}_{2j}$, $\bar{N}_{3j}$, $\bar{\kappa}_{2j}$, $\bar{\kappa}_{3j}$, $\bar{p}_{1j}$, $\bar{p}_{2j}$, $\bar{p}_{3j}$, q_{0j}, q_{1j}, q_{2j}, q_{3j} and $(n-1)$ jumped boundary conditions for $\bar{\kappa}_{1j}$. These boundary conditions together with those provided by Eqs. (12) and (13) produce a well-posed BVP for the multi-rod system, which can be solved using various numerical continuation methods. Here, the Continuation Core and Toolboxes (COCO) [36,37] operated in MATLAB is used. In the numerical implementation, the bending angle θ is set as the continuation parameter, which varies from 0 to π. After the governing equation systems are solved, the bending moment needed to prescribe the bending angle θ equals the internal moment at the loading points, which is given by

$$\bar{M} = \frac{MR_0}{GJ} = \frac{M_{3m}R_0}{GJ} = \bar{\kappa}_{3m} \tag{14}$$

3 Snap-Folding of Single-Layer Curved Rings

In this section, the influences of segment curvature on folded configurations of single-layer curved polygonal rings and their corresponding packing ratios are studied based on FEA simulations and the rod model. We first study single-layer curved hexagonal rings that can fold into fully overlapping configurations. Figure 3(*a*) shows the initial and folded configurations of single-layer hexagonal rings with different segment curvatures (see Movie 2 available in the Supplemental Materials for the folding processes). The normalized segment curvature is defined as R_0/R_n, where R_0 is the radius of the circumcircle of the ring and R_n is the natural radius of the ring segment in the deployed, unstressed state, with R_n being negative or positive. From here on, rings with negative R_n will be referred to as concave (curved inwards) while those with positive R_n will be referred to as convex (curved outward). Note that the use of the terminology concave or convex does not refer to the convexity of the ring itself. Here, single-layer hexagonal rings with six normalized natural curvatures (with the same R_0) ranging from -2.1 to 3 are studied. The rings with $R_0/R_n = -2.1$ and 3 are two extreme cases where the adjacent segments of the rings merge with a common tangent or cusp. When $R_0/R_n = 0$, the hexagonal ring with straight segments (corresponding to $R_n = \infty$) folds into a three-loop overlapping peach core structure, which has been reported in our previous work [13,15]. Interestingly, for concave cases, as the segment curvature decreases from 0 to a critical value of -1.8, the folded state gradually transforms from a peach core shape to a three-loop straight-line configuration which has the smallest area among all folded states of the curved hexagonal rings studied here. This critical segment curvature ($R_0/R_n = -1.8$) is equal to the segment curvature of the peach core-shaped configuration folded from a hexagonal ring with straight segments ($R_0/R_n = 0$). Continuing to decrease the segment curvature results in a folded configuration whose top and bottom segments intersect with each other (e.g., $R_0/R_n = -2.1$). For convex cases, the folded states change from a peach core shape to a peanut shape (e.g., $R_0/R_n = 2$) upon increasing the segment curvature from $R_0/R_n = 0$. Interestingly, we find that the hexagonal ring with $R_0/R_n = 3$ no longer folds into an overlapping configuration. Instead, it inverts via torsional rotation around the entire ring from a ring with convex segments to a ring with concave segments. Note that a three-loop configuration of this ring is still achievable by imposing additional constraints on the ring during folding. This multistable behavior is worth further investigation but will not be the focus of this paper.

Variations of the normalized moment (MR_0/GJ) with respect to the bending angle (θ) for a series of hexagonal rings, predicted by the FEA simulations and the rod model, are plotted in Fig. 3(*b*). The theoretical results match the FEA results with good accuracy. The peak of each curve is the snapping point, i.e., the point where snap-folding is triggered. Upon applying a bending angle, θ, and after reaching the snapping point, the ring folds to its final configuration in a self-guided manner. It can be observed that the

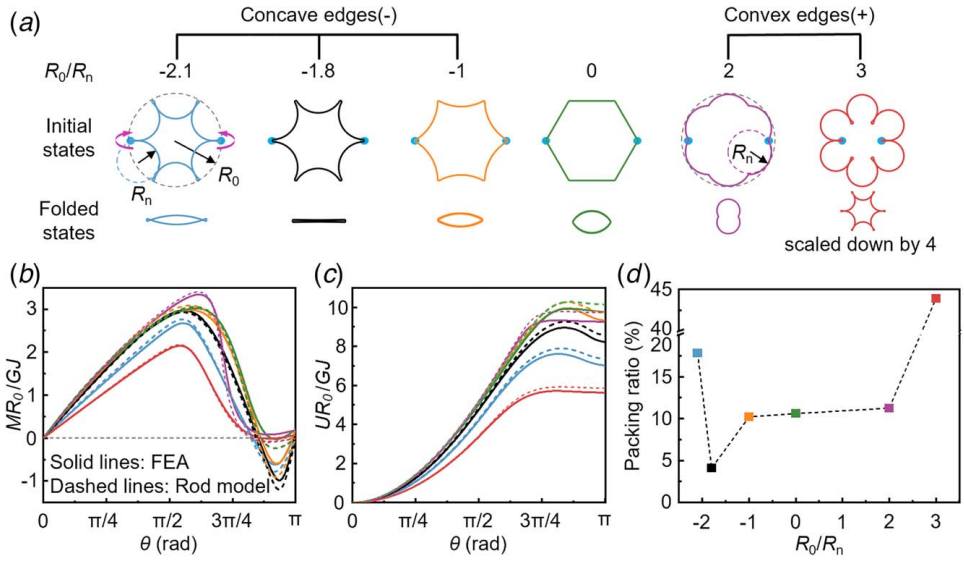

Fig. 3 Snap-folding of single-layer hexagonal rings with different segment curvatures under bending applied at corners. (*a*) Initial states and folded states of single-layer hexagonal rings with different segment curvatures. The blue dots denote the bending locations. FEA and theoretical results of (*b*) normalized moment-bending angle curves and (*c*) normalized strain energy-bending angle curves for single-layer hexagonal rings. (*d*) Packing ratios of single-layer hexagonal rings with different segment curvatures.

maximum moment for the ring with $R_0/R_n = 3$ is the lowest among various hexagonal rings. This is because it merely needs to invert, or "turn inside out", instead of folding to a multiloop overlapping state. Figure 3(*c*) shows the relationship between the normalized strain energy (UR_0/GJ) and the bending angle (θ) for single-layer hexagonal rings with different segment curvatures during the folding process. We find that the strain energy obtained from FEA agrees well with that evaluated by the rod model. Specifically, each energy curve of the hexagonal rings shows two local minimum points: one is located at $\theta = 0$, corresponding to the initial state, and the other is near $\theta = \pi$, corresponding to the folded state, indicating a bistable elastic folding behavior. Figure 3(*d*) compares the calculated packing ratios of hexagonal rings with different segment curvatures. Here, the packing ratio is defined as the area ratio of the folded configuration to the initial configuration. Benefitting from its straight-line folded configuration, the hexagonal ring having concave segments with $R_0/R_n = -1.8$ exhibits the best packing ability with a packing ratio of 4.1%, which is 2.5 times smaller than that of the hexagonal ring with straight segments (10.6%). By contrast, the hexagonal ring having convex segments

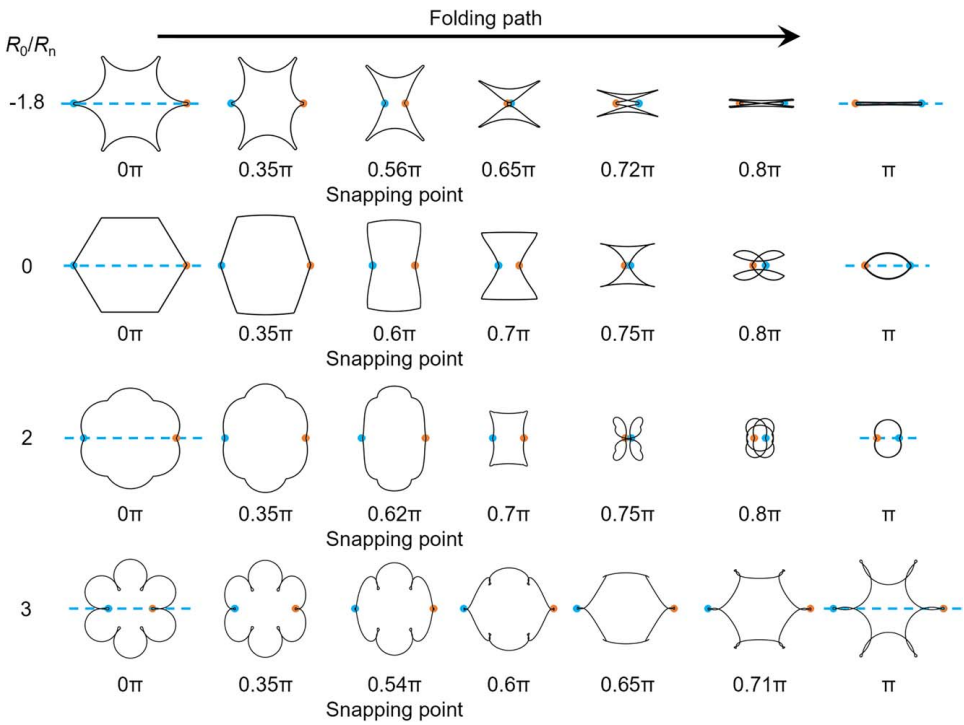

Fig. 4 Snap-folding paths of single-layer hexagonal rings with different segment curvatures. The blue and orange dots denote the bending locations.

with $R_0/R_n = 3$ (whose segments meet at a cusp) has a packing ratio of 43.9% since its folded configuration is still a single-loop geometry. As the segment curvature varies from −1.8 to 2, the packing ratio increases from 4.1% to 11.3%. Therefore, the packing efficiency of a hexagonal ring can be improved by introducing concave segments with appropriate curvature. Folding paths of hexagonal rings with several different segment curvatures under bending loads are illustrated in Fig. 4. It is seen that the rings rapidly reduce in size after the snapping point is reached. For the hexagonal ring with $R_0/R_n = 3$, unlike the other rings that fold into a three-loop overlapping configuration, it inverts into a single-loop geometry that is similar to the concave hexagonal ring. As mentioned earlier, the three-loop configuration is achievable by imposing additional constraints during folding.

Next, we study the effect of segment curvature on the folded configurations and packing ratios of single-layer curved octagonal rings. Unlike hexagonal rings, octagonal rings cannot fold into fully overlapping three-loop configurations as their segment number are not $3n$, where n is an integer greater than or equal to 2 [12,15]. Initial and folded configurations of six octagonal rings with different segment curvatures are presented in Fig. 5(*a*) (see Movie 3 available in the Supplemental Materials for the folding processes), in which the rings with $R_0/R_n = -2.87$ and 3.63 are the two extreme cases where their adjacent curved segments form cusps. It is seen that the octagonal ring with straight segments ($R_0/R_n = 0$) folds into a wreath shape. For the concave segments with curvature decreasing from 0 to –1.94, the folded configurations of the curved octagonal rings change from a wreath shape to an octagram. For the convex segments, the ring with $R_0/R_n = 2$ folds into a more compact wreath shape. For the two extreme cases, $R_0/R_n = -2.87$ and 3.63, the curved octagonal rings invert and retain their single-loop form but reverse their segment curvatures from concave to convex and vice versa.

Figures 5(*b*) and 5(*c*) show the normalized moment-bending angle curves and the normalized strain energy-bending angle curves for single-layer octagonal rings with different segment curvatures, respectively. It is seen from Fig. 5(*b*) that all six rings exhibit the snap-folding behavior described earlier. Similar to what was observed for the curved hexagonal rings, the maximum moments for the two extreme cases ($R_0/R_n = -2.87$ and 3.63) are much lower than those of the other geometries. Moreover, the energy landscapes indicate that all the rings are stable at both their initial and folded states. In other words, the rings display bistable elastic folding.

The packing ratios of single-layer octagonal rings are illustrated in Fig. 5(*d*). Among the six different segment curvatures considered, the curved octagonal ring with $R_0/R_n = 2$ exhibits the best packing ability with a ratio of 12.9%, which is slightly lower than that of the octagonal ring with straight segments (13.4%). As the segment curvature decreases from 2 to −1.94, the packing ratio of the single-layer octagonal rings gradually increases from 12.9% to 17.2%. This indicates that the curved octagonal rings tend to have better packing ability when their segments are convex, contrary to the single-layer curved hexagonal rings. The two curved octagonal rings whose tangent segments merge as cusps ($R_0/R_n = -2.87$ and 3.63) have packing efficiencies much lower than the other octagonal rings, because their inverted shapes are single-looped. In Fig. 6, folding paths are illustrated for single-layer octagonal rings with various segment curvatures under bending loads. It is seen that the octagonal rings with $R_0/R_n = -1.94$, 0, and 2 snap-fold into much smaller sized configurations once the bending angle passes the snapping point, while the sizes of the two curved octagonal rings with $R_0/R_n = -2.87$ and 3.63 change minimally during folding.

4 Snap-Folding of Double-Layer Curved Rings

In this section, the effects of segment curvature on folded configurations and packing ratios of double-layer curved rings are examined based on FEA simulations. Here, double-layer rings are continuous rods with two loops stacked on one another, which can be obtained by coiling a disconnected ring by π and then reconnecting it (see Appendix B for details on double-layer square rings). We first study the snap-folding behaviors of double-layer curved square rings that can fold into fully overlapping folded configurations under bending loads. Note that the bending loads are applied at the left corners of both layers. In Fig. 7(*a*), the initial and folded states of the double-layer square rings with six different segment curvatures varying from −1.28 to 2.42 are presented (see

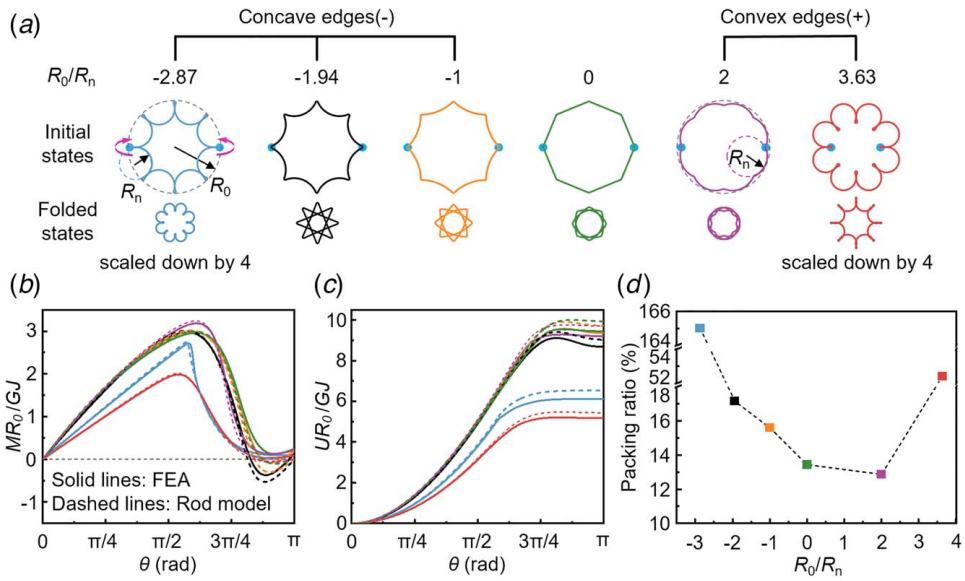

Fig. 5 Snap-folding of single-layer octagonal rings with different segment curvatures under applied bending loads at corners. (*a*) Initial states and folded states of single-layer octagonal rings with various segment curvatures. The blue dots denote the bending locations. FEA and theoretical results of (*b*) normalized moment-bending angle curves and (c) normalized strain energy-bending angle curves for single-layer curved octagonal rings. (*d*) Packing ratios of single-layer octagonal rings with various segment curvatures.

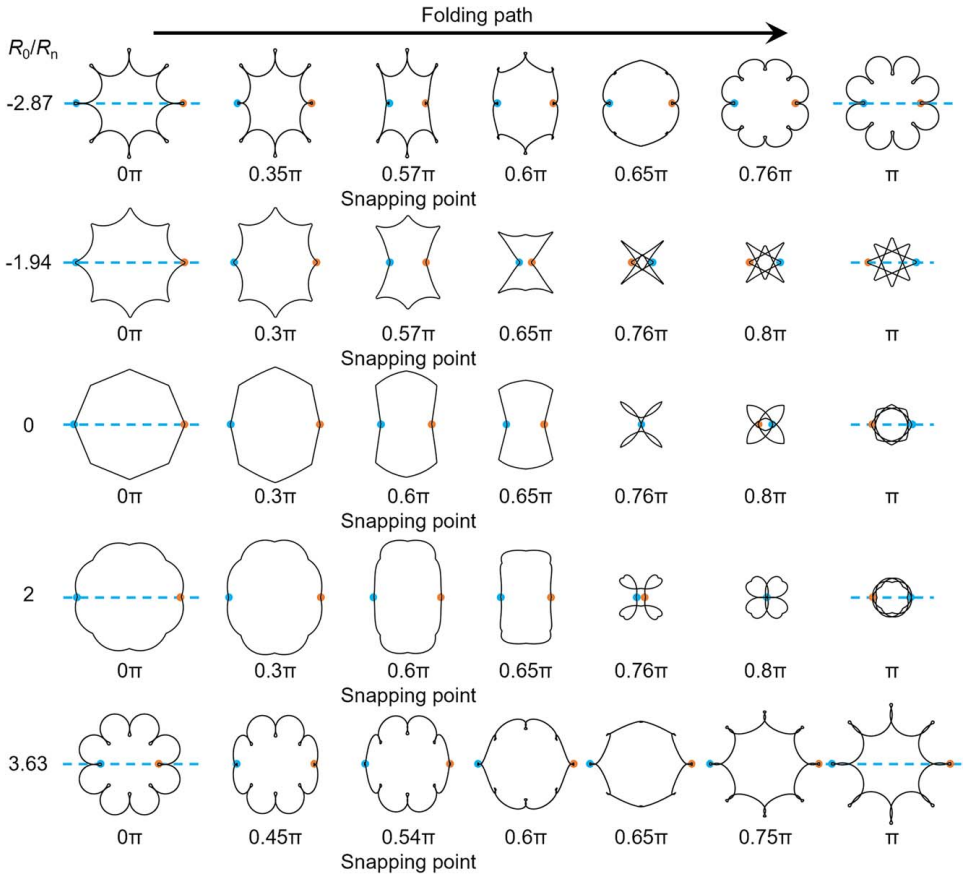

Fig. 6 Snap-folding paths of single-layer octagonal rings with various segment curvatures. The blue and orange dots denote the bending locations.

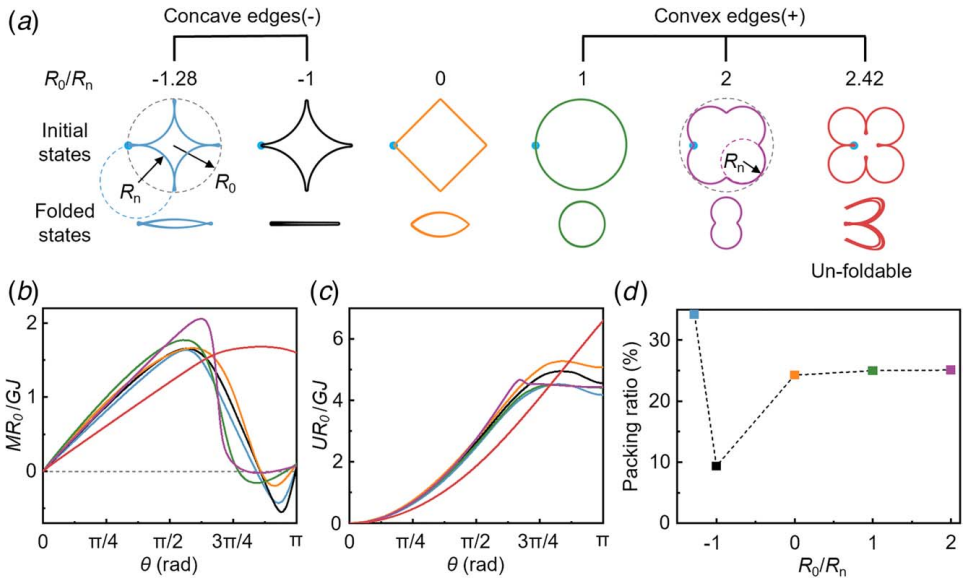

Fig. 7 Snap-folding of double-layer square rings with six different segment curvatures under bending loads. (*a*) Initial states and folded states of double-layer square rings with different segment curvatures. The bending loads are applied at the left corners of both layers, which are denoted by blue dots. FEA results of (*b*) normalized moment-bending angle curves and (*c*) normalized strain energy-bending angle curves for double-layer square rings with different segment curvatures. (*d*) Packing ratios of double-layer square rings with different segment curvatures.

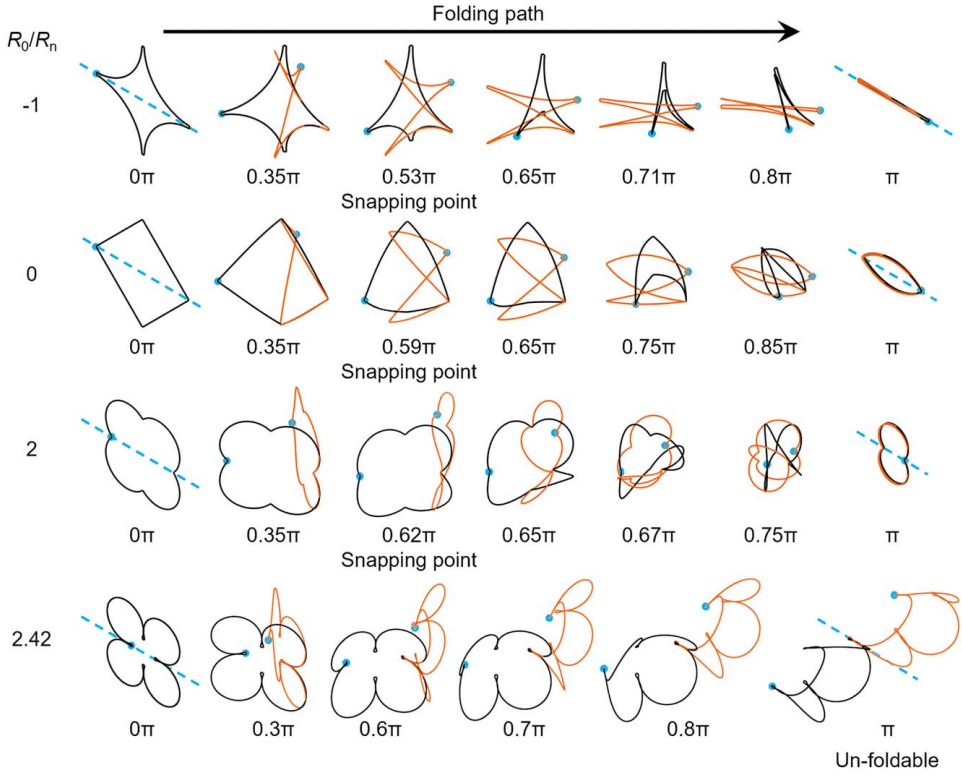

Fig. 8 Isometric views of the folding paths of the double-layer square rings with different segment curvatures. The bending loads are applied at the left corners of both layers, and the bending locations are denoted by blue dots.

Movie 4 available in the Supplemental Materials for the folding processes), in which rings with $R_0/R_n = -1.28$ and 2.42 are two extreme cases where their adjacent tangent curved segments form cusps. It is found that the double-layer square ring with straight segments ($R_0/R_n = 0$) can fold into a four-loop overlapping peach core configuration. This is different than the case of a single-layer square ring, which has a non-fully overlapping cross-shaped folded configuration [12,15]. As the segment curvature decreases, the folded configuration of the double-layer square ring with concave segments gradually flattens. Particularly, the ring with $R_0/R_n = -1$ folds into

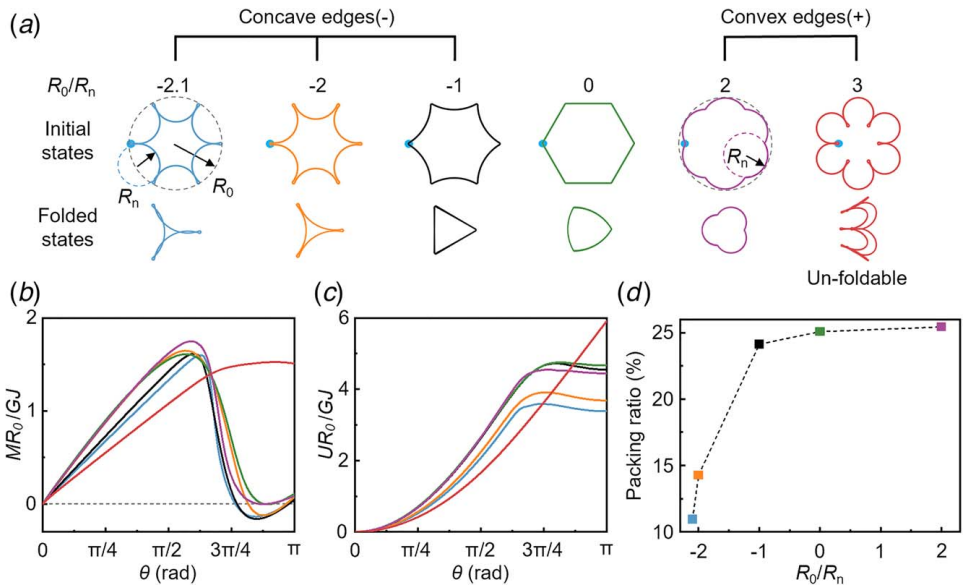

Fig. 9 Snap-folding of double-layer hexagonal rings with different segment curvatures under bending loads. (*a*) Initial states and folded states of double-layer hexagonal rings with different segment curvatures. The bending loads are applied at the left corners of both layers, and the bending locations are denoted by blue dots. FEA results of (*b*) normalized moment-bending angle curves and (c) normalized strain energy-bending angle curves for double-layer hexagonal rings with different segment curvatures. (*d*) Packing ratios of double-layer hexagonal rings with different segment curvatures.

a highly compact four-loop straight-line configuration with the smallest packing area. When the segment curvature continues to decrease, the top and bottom segments of the straight-line loop begin to intersect with each other. By contrast, when increasing the segment curvature to 1, the initial state of the double-layer square ring turns into a double-layer circular ring, which folds into a four-loop circular ring with half the radius of its initial configuration. With the segment curvature changing from 1 to 2, the folded configuration gradually changes from a circle to a peanut shape. Lastly, for the convex ring with adjacent segments tangent to one another ($R_0/R_n = 2.42$), the double-layer square ring is no longer observed to be foldable and deforms into an unstable 3D configuration.

Variations of the normalized moment (MR_0/GJ) with respect to the bending angle (θ) for double-layer square rings with various segment curvatures are shown in Fig. 7(*b*). For rings with segment curvatures from −1.28 to 2, the normalized moment first increases to the snapping point and then decreases below zero, revealing that these five rings undergo snap-folding behavior. For the double-layer square ring with $R_0/R_n = 2.42$, however, the normalized moment does not decrease towards zero after passing the peak point, suggesting that the ring is unfoldable. Figure 7(*c*) illustrates the relationship between the normalized strain energy (UR_0/GJ) and bending angle (θ) for the double-layer square rings with different segment curvatures. For the five rings exhibiting snap-folding behavior, their energy curves have two local minima at $\theta = 0$ and near $\theta = \pi$, which means both the initial and folded states of these rings are stable. However, the strain energy of the ring with $R_0/R_n = 2.42$ monotonically increases as the bending angle varies from 0 to π, revealing that the ring is only stable at its initial state. The packing ratios of double-layer square rings with different segment curvatures are shown in Fig. 7(*d*). As expected, the double-layer square ring with segment curvature $R_0/R_n = -1$ possesses the best packing ability due to its straight-line configuration, whose packing ratio is only 9.4%. We can also see that the packing ratio of the double-layer square ring rapidly increases from 9.4% to 24.2% as the segment curvature changes from −1 to 0, while it nearly remains unchanged when increasing the segment curvature from 0 to 2. Therefore, the packing ability of the double-layer square ring can be effectively improved by introducing concave segments with a relatively small curvature. For the double-layer square ring with $R_0/R_n = -1.28$, it has the lowest packing efficiency with a value of 34.2%. Isometrical views of the folding paths for the double-layer square rings with various segment curvatures under bending loads are shown in Fig. 8, where the front and back layers of the rings are denoted by black and orange, respectively. Note that the bending loads are applied on the left corners of both layers. During folding, the double-layer square rings with $R_0/R_n = -1$, 0, and 2 first bend in opposite directions and then snap-fold to different four-loop fully overlapping geometries. For the double-layer square ring with $R_0/R_n = 2.42$, it can only be reconfigured to an unstable 3D configuration when the bending angle increases from 0 to π.

Finally, we investigate the influence of segment curvature on the folded configurations and packing ratios of double-layer hexagonal rings. Figure 9(*a*) shows the initial and folded configurations of double-layer hexagonal rings with different segment curvatures (see Movie 5 available in the Supplemental Materials for the folding processes). Here, six different segment curvatures varying from −2.1 to 3 are considered, with segment curvatures $R_0/R_n = -2.1$ and 3 corresponding to cases where adjacent segments of the rings are tangent. It is seen that the double-layer hexagonal ring with straight segments ($R_0/R_n = 0$) folds into a four-loop triangle with convex segments, instead of folding into a three-loop peach core shape like the single-layer hexagonal ring. When the segment curvature decreases from 0 to −2, the folded configurations of the rings change from a convex triangle ($R_0/R_n = 0$) to an equilateral triangle ($R_0/R_n = -1$) and then to a concave triangle ($R_0/R_n = -2$).

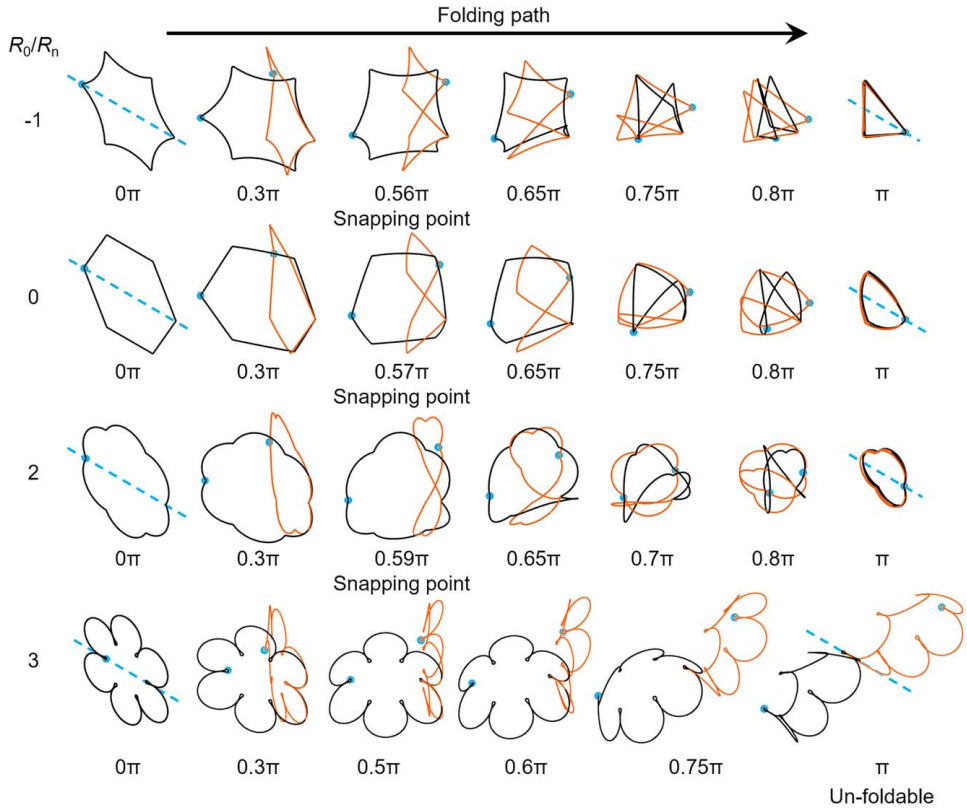

Fig. 10 Isometric views of the folding paths of double-layer hexagonal rings with different segment curvatures under bending loads. The bending loads are applied at the left corners of both layers, and the bending locations are denoted by blue dots.

For the double-layer hexagonal ring with $R_0/R_n = -2.1$, it folds into a triangle with intersected adjacent segments and has the smallest area among the various folded configurations. For double-layer hexagonal rings with convex segments, the ring folds into a geometry with three rounded segments when $R_0/R_n = 2$, but it appears to become unfoldable when $R_0/R_n = 3$.

Variations of the normalized moment and the normalized strain energy with respect to the bending angle for the six different double-layer hexagonal rings during their folding processes are presented in Figs. 9(*b*) and 9(*c*), respectively. It is seen from Fig. 9(*b*) that the double-layer hexagonal rings, with segment curvatures from −2.1 to 2, fold from their initial states to the final states via the snap-through instability. The energy curves in Fig. 9(*c*) show that both the initial and folded states of these rings are stable, which implies that they experience bistable elastic folding behaviors. Also, we can find that the double-layer hexagonal ring with $R_0/R_n = 3$ is unfoldable, as its normalized strain energy monotonically increases as the bending angle increases. Figure 9(*d*) compares the packing ratios of the five foldable double-layer hexagonal rings. It is seen that the ring with tangent concave segments ($R_0/R_n = -2.1$) shows the best packing ability, as its folded configuration is only 11% of its initial area. As the segment curvature increases from −2.1 to −1, the packing ratio rapidly increases from 11% to 24.1%, while it only increases slightly from 24.1% to 25.1% when the segment curvature increases from −1 to 2. Therefore, for double-layer hexagonal rings, introducing concave segments with a relatively large curvature can result in a higher packing efficiency. The isometric views of the folding paths of double-layer hexagonal rings with different segment curvatures under bending loads are shown in Fig. 10. One can find that for $R_0/R_n = -1$, 0, and 2, the rings undergo a similar folding process from their initial states to the four-loop overlapping states. For $R_0/R_n = 3$, however, the double-layer hexagonal ring with tangent convex segments can only fold to an unstable 3D configuration.

5 Conclusion

In this work, we have studied the effects of segment curvature on the snap-folding and packing abilities of curved ring origami based on a combination of experiments, finite element analysis, and theoretical modeling. Four types of curved ring origami have been considered: single-layer hexagonal rings and octagonal rings, as well as double-layer square rings and hexagonal rings. The observations and associated calculations indicate that segment curvature has a significant influence on the folded configurations and packing abilities of curved ring origami. An unusually rich variety of behavior has been observed in our experiments, and we readily admit that this study has not been exhaustive. Nevertheless, we hope the reported results will prompt further study of the phenomena and stimulate applications in relevant fields.

For the single-layer hexagonal ring and double-layer square and hexagonal rings, their packing abilities can be significantly improved by introducing concave segments with appropriate segment curvatures, due to the fully overlapping folded states achievable. Particularly, the single-layer hexagonal rings and double-layer square rings can fold into straight-line loop configurations when their normalized segment curvatures equal −1.8 and −1, respectively. Their unique folded configurations also enable the highest packing efficiency for single-layer rings and double-layer rings, with a value of 4.1% and 9.4%, respectively. Although inverting behavior is preferred over folding for the convex hexagonal ring with large curvature, the fully overlapping folded state is still achievable when imposing additional constraints during folding. For single-layer octagonal rings, however, they cannot fold into fully overlapping states and their packing ability tends to only improve slightly when convex segments are introduced. It is expected that the proposed curved ring origami can provide a new perspective for the design of foldable and deployable structures with simple folded configurations and high packing efficiency with great potential in applications including deployable aerospace structures, foldable electronics, and reconfigurable architecture.

Acknowledgment

R.R.Z., J.D., L.L, and S.L. acknowledge National Science Foundation Award CPS-2201344 and National Science Foundation Career Award CMMI-2145601 for the support of this work.

Conflict of Interest

There are no conflicts of interest.

Data Availability Statement

The data sets generated and supporting the findings of this article are obtainable from the corresponding author upon reasonable request.

Appendix A. Folded Configurations of Polygonal Rings

Figure 11 shows the folded configurations of various polygonal rings. It is seen that polygonal rings can only fold into three-loop fully overlapping configurations when the segment number of the polygonal rings equals 3*n* (*n* must be an integer greater than or equal to 2).

Appendix B. Fabrication of Curved Rings

The rings in Fig. 1 are fabricated by manually reshaping stainless steel wires and connecting the two ends. To create a double-layer square ring, we first disconnect a single-layer octagonal ring, and then coil it into two loops, as shown in Fig. 12. Finally, we connect both ends of the disconnected ring to form a double-layer square ring.

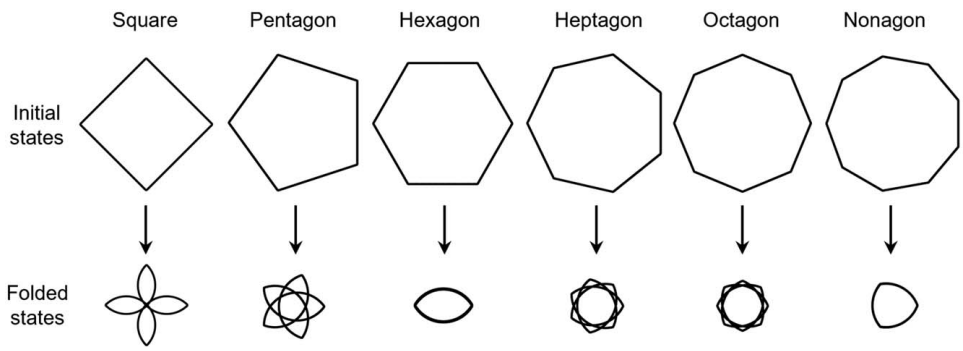

Fig. 11 Initial and folded states of various polygonal rings

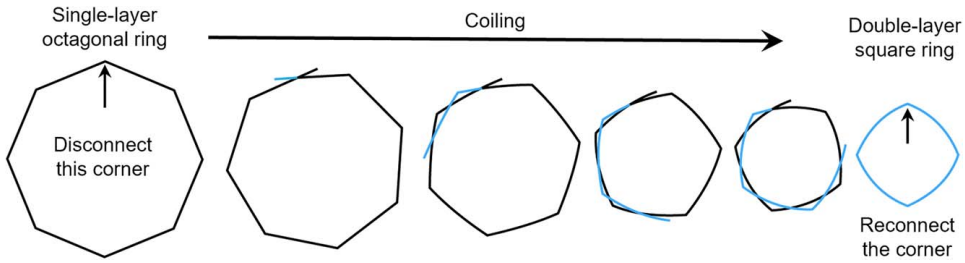

Fig. 12 Fabrication process of a double-layer square ring coiled from a single-layer octagonal ring. The blue color denotes the second layer.

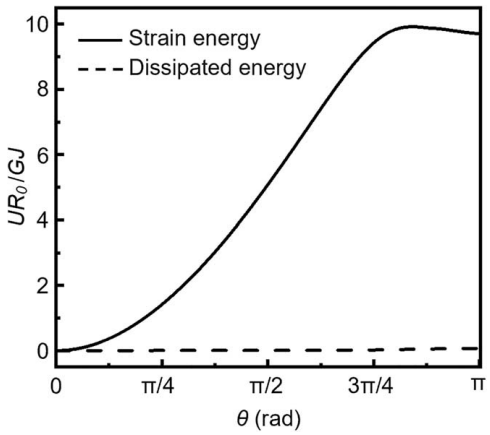

Fig. 13 Normalized strain energy and dissipated energy during folding of a hexagonal ring with straight segments

Appendix C. Energy Dissipation in FEA

For all FEA simulations in ABAQUS, a small damping factor of 10^{-8} is added to stabilize the buckling simulations of the rings. The corresponding energy dissipation is negligible. For example, Fig. 13 shows the normalized energy-bending angle curves of a hexagonal ring with straight segments during folding. It is seen that the energy dissipation is almost zero compared to the strain energy during folding.

References

[1] Pellegrino, S., 2001, "Deployable Structures in Engineering," *Deployable Structures*, Springer, E, pp. 1–35.
[2] Guest, S., and Pellegrino, S., 1996, "A New Concept for Solid Surface Deployable Antennas," Acta Astronaut., **38**(2), pp. 103–113.
[3] Ze, Q., Wu, S., Nishikawa, J., Dai, J., Sun, Y., Leanza, S., Zemelka, C., Novelino, L. S., Paulino, G. H., and Zhao, R. R., 2022, "Soft Robotic Origami Crawler," Sci. Adv., **8**(13), p. eabm7834.
[4] Wu, S., Ze, Q., Dai, J., Udipi, N., Paulino, G. H., and Zhao, R., 2021, "Stretchable Origami Robotic Arm With Omnidirectional Bending and Twisting," Proc. Natl. Acad. Sci., **118**(36), p. e2110023118.
[5] Chen, Q., Feng, F., Lv, P., and Duan, H., 2022, "Origami Spring-Inspired Shape Morphing for Flexible Robotics," Soft Rob., **9**(4), pp. 798–806.
[6] Kuribayashi, K., Tsuchiya, K., You, Z., Tomus, D., Umemoto, M., Ito, T., and Sasaki, M., 2006, "Self-Deployable Origami Stent Grafts as a Biomedical Application of Ni-Rich TiNi Shape Memory Alloy Foil," Mater. Sci. Eng. A, **419**(1–2), pp. 131–137.
[7] Mhatre, S., Boatti, E., Melancon, D., Zareei, A., Dupont, M., Bechthold, M., and Bertoldi, K., 2021, "Deployable Structures Based on Buckling of Curved Beams Upon a Rotational Input," Adv. Funct. Mater., **31**(35), p. 2101144.
[8] Liu, Y., Yan, Z., Lin, Q., Guo, X., Han, M., Nan, K., Hwang, K. C., Huang, Y., Zhang, Y., and Rogers, J. A., 2016, "Guided Formation of 3D Helical Mesostructures by Mechanical Buckling: Analytical Modeling and Experimental Validation," Adv. Funct. Mater., **26**(17), pp. 2909–2918.
[9] Xu, Z., Fan, Z., Zi, Y., Zhang, Y., and Huang, Y., 2020, "An Inverse Design Method of Buckling-Guided Assembly for Ribbon-Type 3d Structures," ASME J. Appl. Mech., **87**(3), p. 031004.
[10] Wu, S., Yue, L., Jin, Y., Sun, X., Zemelka, C., Qi, H. J., and Zhao, R., 2021, "Ring Origami: Snap-Folding of Rings With Different Geometries," Adv. Intell. Syst., **3**(9), p. 2100107.
[11] Yoshiaki, G., Yasuhito, W., Toshihiro, K., and Makoto, O., 1992, "Elastic Buckling Phenomenon Applicable to Deployable Rings," Int. J. Solids Struct., **29**(7), pp. 893–909.
[12] Lu, L., Leanza, S., and Zhao, R. R., 2023, "Origami with Rotational Symmetry: A Review on Their Mechanics and Design," ASME Appl. Mech. Rev., **75**(5), p. 050801.
[13] Wu, S., Dai, J., Leanza, S., and Zhao, R. R., 2022, "Hexagonal Ring Origami—Snap-Folding With Large Packing Ratio," Extreme Mech. Lett., **53**, p. 101713.
[14] Lu, L., Leanza, S., Dai, J., Sun, X., and Zhao, R. R., 2023, "Easy Snap-Folding of Hexagonal Ring Origami by Geometric Modifications," J. Mech. Phys. Solids, **171**, p. 105142.
[15] Leanza, S., Wu, S., Dai, J., and Zhao, R. R., 2022, "Hexagonal Ring Origami Assemblies: Foldable Functional Structures With Extreme Packing," ASME J. Appl. Mech., **89**(8), p. 081003.
[16] Chen, T., Bilal, O. R., Lang, R., Daraio, C., and Shea, K., 2019, "Autonomous Deployment of a Solar Panel Using Elastic Origami and Distributed Shape-Memory-Polymer Actuators," Phys. Rev. Appl., **11**(6), p. 064069.
[17] Yan, Z., Wang, K., and Wang, B., 2022, "Buckling of Circular Rings and its Applications in Thin-Film Electronics," Int. J. Mech. Sci., **228**, p. 107477.
[18] Mouthuy, P.-O., Coulombier, M., Pardoen, T., Raskin, J.-P., and Jonas, A. M., 2012, "Overcurvature Describes the Buckling and Folding of Rings From Curved Origami to Foldable Tents," Nat. Commun., **3**(1), pp. 1–8.
[19] Sun, X., Wu, S., Dai, J., Leanza, S., Yue, L., Yu, L., Jin, Y., Qi, H. J., and Zhao, R. R., 2022, "Phase Diagram and Mechanics of Snap-Folding of Ring Origami by Twisting," Int. J. Solids Struct., **248**, p. 111685.
[20] Leanza, S., Zhao, R. R., and Hutchinson, J. W., 2023, "On the Elastic Stability of Folded Rings in Circular and Straight States," Eur. J. Mech. - A/Solids.
[21] Kaczmarski, B., Moulton, D. E., Kuhl, E., and Goriely, A., 2022, "Active Filaments I: Curvature and Torsion Generation," J. Mech. Phys. Solids, **164**, p. 104918.
[22] Tong, D., Choi, A., Joo, J., Borum, A., and Khalid Jawed, M., 2023, "Snap Buckling in Overhand Knots," ASME J. Appl. Mech., **90**(4), p. 041008.
[23] Dias, M. A., Dudte, L. H., Mahadevan, L., and Santangelo, C. D., 2012, "Geometric Mechanics of Curved Crease Origami," Phys. Rev. Lett., **109**(11), p. 114301.
[24] Manning, R. S., and Hoffman, K. A., 2001, "Stability of n-Covered Circles for Elastic Rods With Constant Planar Intrinsic Curvature," J. Elast., **62**(1), pp. 1–23.
[25] Audoly, B., and Seffen, K. A., 2015, "Buckling of Naturally Curved Elastic Strips: The Ribbon Model Makes a Difference," J. Elast., **119**(1–2), pp. 293–320.
[26] Dias, M. A., and Audoly, B., 2014, "A Non-Linear Rod Model for Folded Elastic Strips," J. Mech. Phys. Solids, **62**, pp. 57–80.
[27] Yu, T., Marmo, F., Cesarano, P., and Adriaenssens, S., 2023, "Continuous Modeling of Creased Annuli With Tunable Bistable and Looping Behaviors," Proc. Natl. Acad. Sci. U. S. A., **120**(4), p. e2209048120.
[28] Sano, T. G., Pezzulla, M., and Reis, P. M., 2022, "A Kirchhoff-Like Theory for Hard Magnetic Rods Under Geometrically Nonlinear Deformation in Three Dimensions," J. Mech. Phys. Solids, **160**, p. 104739.
[29] Audoly, B., and Pomeau, Y., 2010, *Elasticity and Geometry: From Hair Curls to the Non-Linear Response of Shells*, Oxford University Press, Oxford, UK.
[30] Huang, W., Liu, M., and Hsia, K. J., 2023, "A Discrete Model for the Geometrically Nonlinear Mechanics of Hard-Magnetic Slender Structures," Extreme Mech. Lett., **59**, p. 101977.
[31] Starostin, E., and van der Heijden, G., 2022, "Forceless Folding of Thin Annular Strips," J. Mech. Phys. Solids, **169**, p. 105054.
[32] Timoshenko, S., and Goodier, J. N., 1951, *Theory of Elasticity: by S. Timoshenko and JN Goodier*, McGraw-Hill, New York.
[33] Healey, T. J., and Mehta, P., 2005, "Straightforward Computation of Spatial Equilibria of Geometrically Exact Cosserat Rods," Int. J. Bifurcation Chaos, **15**(03), pp. 949–965.
[34] Yu, T., and Hanna, J., 2019, "Bifurcations of Buckled, Clamped Anisotropic Rods and Thin Bands Under Lateral End Translations," J. Mech. Phys. Solids, **122**, pp. 657–685.
[35] Yu, T., Dreier, L., Marmo, F., Gabriele, S., Parascho, S., and Adriaenssens, S., 2021, "Numerical Modeling of Static Equilibria and Bifurcations in Bigons and Bigon Rings," J. Mech. Phys. Solids, **152**, p. 104459.
[36] Dankowicz, H., and Schilder, F., 2011, "An Extended Continuation Problem for Bifurcation Analysis in the Presence of Constraints," ASME J. Comput. Nonlinear Dyn., **6**(3), p. 031003.
[37] Dankowicz, H., and Schilder, F., 2013, *Recipes for Continuation*, Society for Industrial and Applied Mathematics, Philadelphia, PA.